



Article

# A Low-Power SAR ADC with Capacitor-Splitting Energy-Efficient Switching Scheme for Wearable Biosensor Applications

Yunfeng Hu <sup>1,\*</sup>, Qingming Huang <sup>1</sup>, Bin Tang <sup>1</sup>, Chaoyi Chen <sup>1</sup>, Lexing Hu <sup>1</sup>, Enhao Yu <sup>1</sup>, Bin Li <sup>2</sup> and Zhaohui Wu <sup>2</sup>

<sup>1</sup> Zhongshan Institute, University of Electronic Science and Technology of China, Zhongshan 528402, China

<sup>2</sup> School of Microelectronics, South China University of Technology, Guangzhou 510640, China

\* Correspondence: huyf@zsc.edu.cn

**Abstract:** A low-power SAR ADC with capacitor-splitting energy-efficient switching scheme is proposed for wearable biosensor applications. Based on capacitor-splitting, additional reference voltage  $V_{cm}$ , and common-mode techniques, the proposed switching scheme achieves 93.76% less switching energy compared to the conventional scheme with common-mode voltage shift in one LSB. With the switching scheme, the proposed SAR ADC can lower the dependency on the accuracy of  $V_{cm}$  and the complexity of digital control logic and DAC driver circuits. Furthermore, the SAR ADC employs low-noise and low-power dynamic comparators utilizing multi-clock control, low sampling error sampling switches based on the bootstrap technique, and dynamic SAR logic. The simulation results demonstrate that the ADC achieves a 61.77 dB SNDR and a 78.06 dB SFDR and consumes 4.45  $\mu$ W of power in a 180 nm process with a 1 V power supply, a full-swing input signal frequency of 93.33 kHz, and a sampling rate of 200 kS/s.

**Keywords:** SAR ADC; capacitor-splitting; common-mode shift; low complexity



**Citation:** Hu, Y.; Huang, Q.; Tang, B.; Chen, C.; Hu, L.; Yu, E.; Li, B.; Wu, Z. A Low-Power SAR ADC with Capacitor-Splitting Energy-Efficient Switching Scheme for Wearable Biosensor Applications. *Micromachines* **2023**, *14*, 2244.

<https://doi.org/10.3390/mi14122244>

Academic Editor: Antonella Battisti

Received: 9 November 2023

Revised: 10 December 2023

Accepted: 14 December 2023

Published: 15 December 2023



**Copyright:** © 2023 by the authors. Licensee MDPI, Basel, Switzerland. This article is an open access article distributed under the terms and conditions of the Creative Commons Attribution (CC BY) license (<https://creativecommons.org/licenses/by/4.0/>).

## 1. Introduction

The rapid development of wireless sensors, portable electronic devices, and biomedical systems has led to ever-increasing performance needs for ADCs utilized in sensor interfaces, wearable medical devices, and other areas [1]. Among them, wearable biosensor applications have attracted more attention, with features such as lightweight, battery-powered or energy-harvesting circuit-powered, and low sampling frequency posing challenges for system design in terms of miniaturization and ultra-low power consumption [2]. Therefore, efforts have been made to develop low-power wearable biosensor applications or portable medical devices to extract and analyze signals [3,4] to efficiently reflect information such as human health status through early detection of biophysical signals. As shown in Figure 1, in a standard front-end readout system, single-ended biophysical potential signals such as nerve signals and electromyographic (EMG) signals are captured and pre-processed by sensors and AFE modules, and the ADC converts the analog signals that have been processed at the previous level into digital signals that can be processed by the CPU. ADCs play a key role in the system and consume a lot of power. Physiological signals are generally weak with frequency components lying between DC to few hundred Hertz and the amplitude varying from millivolt to microvolt. Thus, a moderate speed (sampling rate) converter is enough to handle these signals [5]. The frequency and amplitude ranges of common physiological signals such as electrocardiogram (ECG) signals, electromyography (EMG) signals, electroencephalogram (EEG) signals, and electrocorticography (ECoG) signals are shown in Table 1.

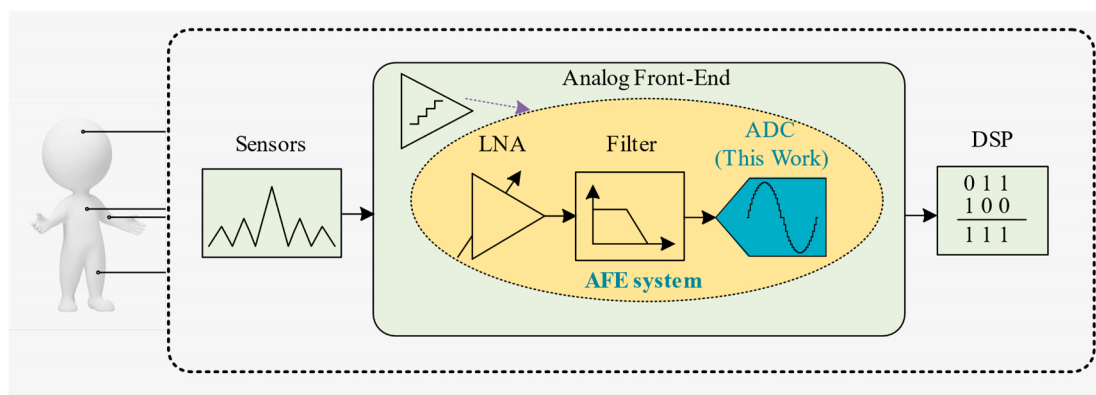


**Figure 1.** Block diagram of a wearable biosensor integrated circuit.

**Table 1.** Physiological signals and its frequency and amplitude ranges [6].

Type of Biological Signals	Frequency Range (Hz)	Amplitude (mV)
ECG	0.01 to 250	0.5 to 4
EMG	Up to 2 K	0.1 to 5
EEG	0.5 to 150	0.0005 to 0.3
ECoG	70 to 110	0.001 to 3

In recent years, the successive approximation register analog-to-digital converter (SAR ADC) has been vigorously developed in the context of the increasing demand for low-power applications due to their simple structure, smaller area, and lower power consumption [1,7–15]. The above advantages justify the use of SAR ADCs as converters in wearable biomedical devices that process physiological signals [6]. Therefore, the design of low-power SAR ADCs has attracted more and more attention, and the innovative designs have achieved higher performance and efficiency in circuits and systems, providing more efficient, high-performance, and high-reliability electronic devices for biosensor applications. In a SAR ADC, the main sources of energy consumption are the capacitive digital-to-analog converters (DACs), comparator, and SAR control logic [16]. The dynamic comparator does not consume static current, and the digital control logic receives benefits from technology scaling. Therefore, the capacitive DAC dominates the overall power consumption [17,18], especially when the resolution increases [19]. The switching energy can be greatly reduced by changing the structure of the capacitor array and the switching method of the capacitors [20].

Several low-power switching schemes have been aggressively introduced to make DACs consume less energy [10–14]. Compared to the conventional architecture [8], the monotonic switching scheme (set and down) based on capacitive top-plate sampling reduces the switching energy loss by 81.26% [9]. Compared to the conventional switching scheme, the  $V_{cm}$ -based switching scheme [10], Wang et al. [11], HSRS [12], SMS [13], and Hu et al. [14] reduce the switching energy by 87.52%, 90.61%, 92.20%, 95.32%, and 95.34%, respectively. The monotonic downward switching scheme is proposed in [9], while  $V_{cm}$  is used in [10] for energy reduction. These DAC structures [10–14] consume substantially less energy, most of them require a high accuracy of  $V_{cm}$  to minimize the resultant error of DACs, or have a large common-mode shift [11–14]. Refs. [10,12,13] rely on three reference levels for each capacitor switch, so the complexity of the logic control of the DAC module is increased, and the difficulty of subsequent circuit implementation is increased, thereby limiting the overall power consumption reduction. Ref. [12] proposed a higher-side-reset-and-set (HSRS) switching scheme with an equally simple and energy efficient logic circuit but with limited energy savings.

To reduce the overall circuit complexity and power consumption of the SAR ADC, a capacitor-splitting low-complexity and energy-efficient DAC switching scheme with one

LSB common-mode shift for SAR ADC has been designed. The capacitor-splitting structure is a method to reduce power and area. In this work, the capacitor-splitting structure, common-mode technique, and  $V_{cm}$  are combined and optimized to achieve the proposed switching scheme. Behavioral simulation of a 10-bit SAR ADC shows 93.76% less switching energy than the conventional method. The  $V_{cm}$ -based tri-level switching scheme is more area-efficient because of the introduction of  $V_{cm}$  (equal to  $V_{ref}/2$ ). Ref. [13] achieved lower switching energy at the cost of high logic complexity. In the proposed switching scheme, only three reference levels are employed for the second least significant bit (Second LSB), while two reference voltages are assigned per capacitor for the remaining capacitors. This design choice significantly reduces the complexity of the capacitance array. Additionally, it is worth noting that the accuracy of  $V_{cm}$  has minimal impact on the accuracy of the digital-to-analog converter (DAC). It only affects the accuracy of the analog-to-digital converter (ADC) in the last two conversion cycles. The common-mode voltage of the capacitor array remains constant except for the LSB conversion, reducing the complexity of the comparator design. Thus, the proposed switching scheme is a good trade-off among switching energy, capacitor area, DAC output common-mode voltage, and ADC accuracy.

Due to the increasing demand for low-power biosensor electronics, many leading-edge switching schemes for DAC capacitor arrays are being applied to SAR ADCs in this field. Ref. [21] describes the design and calibration of an ultra-low power 14-bit 10 KS/s fully differential SAR ADC for biomedical applications. The integrated transient response of the ADC shows a power consumption of only 19.5  $\mu$ W. Ref. [22] presents two low-power design techniques used for SAR ADC for the transmission of a physiological signal: a dual split switching, and a set and reset phase. The power consumption of the SAR ADC is 13.99  $\mu$ W.

To validate the effectiveness and benefits of the proposed scheme, a 10-bit 200 kS/s SAR ADC circuit was simulated and analyzed using a 180 nm CMOS process with a supply voltage of 1 V. The behavioral simulation results revealed that the ADC achieved impressive metrics, including a signal-to-noise and distortion ratio (SNDR) of 61.77 dB, a spurious-free dynamic range (SFDR) of 78.06 dB, and a power consumption of 4.45  $\mu$ W. These achieved metrics meet the requirements of most biosignal applications, showcasing the favorable energy efficiency of the proposed SAR ADC. The results clearly demonstrate the potential of the proposed DAC switching scheme in enhancing the performance of SAR ADCs. The innovation of this work lies in the effective combination of a capacitor-splitting structure and a third reference voltage,  $V_{cm}$ , to achieve a high energy-efficient SAR ADC with a common-mode shift of one least significant bit (LSB) using a common-mode technique.

## 2. Design of the Proposed SAR ADC

The structure of the N-bit SAR ADC is demonstrated in Figure 2. To reduce supply voltage noise and achieve effective common-mode noise rejection, we have implemented the fully differential architecture [23]. The key components of a SAR ADC include the sample-and-hold circuit, the comparator, the capacitive DAC, and successive approximation registers. The capacitive DAC is composed of a positive-phase capacitance array (P cap-array) and a negative-phase capacitance array (N cap-array). Each of these arrays is further divided into three sub-capacitor arrays: high array, low array, and units array. The high array and low array are binary weighted capacitor arrays. Based on the top-plate sampling technique, the analog input is sampled into the ADC through a sample-and-hold circuit. This process is controlled by the sampling switch clock, CLK\_sample. Once the input is sampled, the SAR ADC employs a successive approximation logic algorithm to convert the analog input value into a digital output code. The comparator clock, CLK\_comp, is driven by the reset signal. This clock controls the operation of the comparator, which compares the analog input voltage with the voltage generated by the DAC. The reset signal also triggers the SAR logic to initiate the conversion process, controlling the generation of individual bits. Detailed signaling control details are shown in Figure 2.

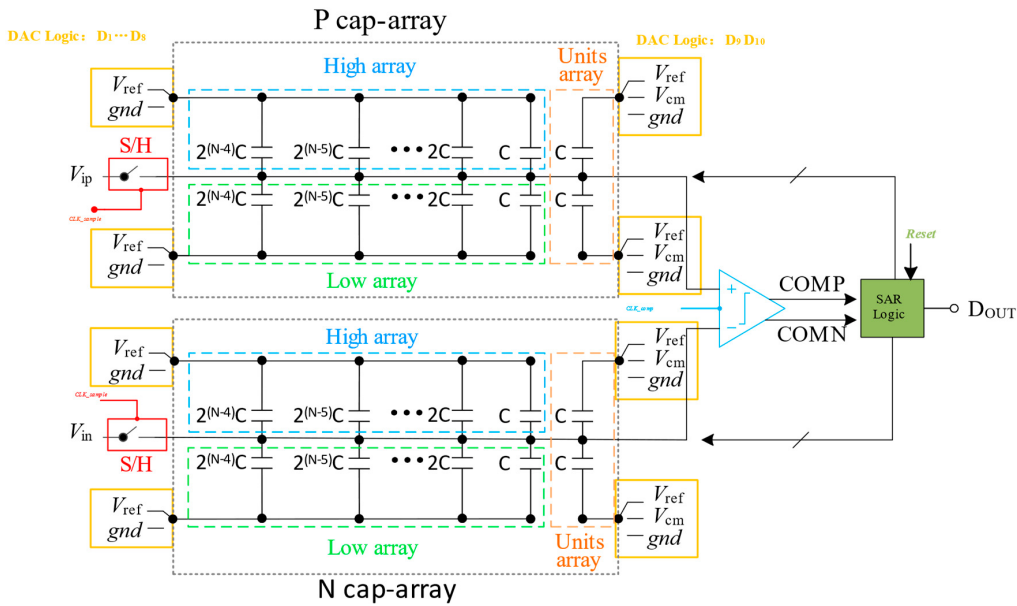


**Figure 2.** The proposed architecture of N-bit SAR ADC.

### 2.1. DAC Switching Scheme

To improve energy efficiency and reduce power consumption, circuit complexity, and occupied area, a novel energy-efficient switching algorithm is proposed for a 4-bit SAR ADC, as illustrated in Figure 3. The gray area in the figure represents the switching of the reference voltage at each conversion stage. In the sampling state, top-plate sampling reduces DAC resolution requirements [9,24,25]. The operation of the ADC can be divided into five phases: sampling and 1st comparison, 2nd to (N – 2)th comparison, (N – 1)th comparison, and Nth comparison.

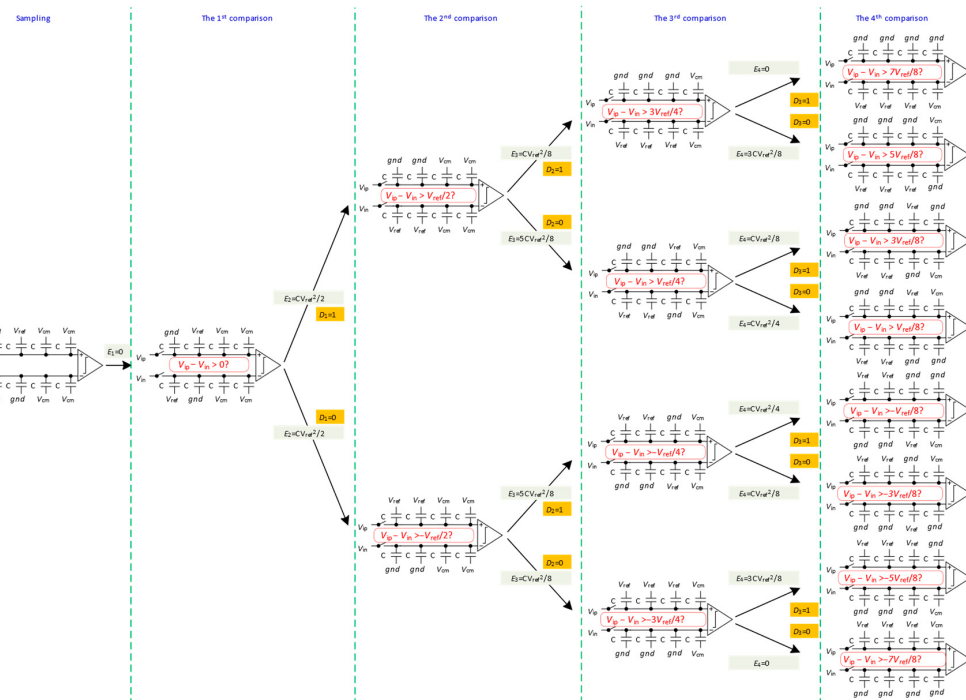


**Figure 3.** Switching procedure of 4-bit SAR DAC.

Sampling and 1st comparison: The input signal is sampled through the sampling switch on the top plates of all capacitors. The bottom plate of the capacitors in the high

array is connected to the reference voltage ( $V_{ref}$ ), the bottom plate of the capacitors in the low array is connected to ground, and the bottom plate of the capacitors in the unit array is connected to the common-mode voltage ( $V_{cm}$ ). After sampling, the sampling switch is turned off, and the comparator performs the initial comparison without using any switching energy. The outcome of this first comparison is denoted as  $D_1$ .

2nd to  $(N - 2)$ th comparison: According to the output of the previous comparison ( $D_{i-1}$ ), the corresponding capacitor in the high array on the high-voltage potential side will be switched from  $V_{ref}$  to ground. Similarly, the corresponding capacitor in the low array on the low-voltage potential side will be switched from ground to  $V_{ref}$ . All other capacitors will remain unchanged. For example, in the second comparison, the largest capacitor in the high array connected to the higher voltage side will be switched from  $V_{ref}$  to ground. Additionally, the largest capacitor in the low array connected to the lower voltage side will be switched from ground to  $V_{ref}$ . The comparator then performs a second comparison and outputs the result of the second comparison ( $D_2$ ). This process continues until the  $(N - 2)$ th comparison is completed. Throughout the switching process, the common-mode voltage remains constant. Based on the capacitive DAC structure, the energy needed to charge and discharge the capacitor is known as the switching energy, and it plays a crucial role in determining the efficiency of different switching schemes. The capacitor array switching energy of the 2nd to  $(N - 2)$ th comparison is as follows:

$$E_i = \left[ (1 - 2D_{i-1}) \sum_{j=1}^{i-1} (2D_j - 1) \cdot 2^{N-i-j-2} + 2^{N-i-2} \right] CV_{ref}^2 \quad (1)$$

$(N - 1)$ th comparison: The first capacitor in the unit array on the higher voltage side switches from  $V_{cm}$  to ground and the first capacitor on the lower voltage side switches from  $V_{cm}$  to  $V_{ref}$ , based on the result of the previous comparator. Then, the comparator performs the comparison and outputs the result ( $D_{N-1}$ ). From this stage onward, the DAC utilizes an additional reference voltage  $V_{cm}$  to perform more bits of conversion, resulting in area savings and increased efficiency. The capacitor array switching energy in the  $(N - 1)$ th comparison is as follows:

$$E_{(N-1)} = \left[ (1 - 2D_{N-2}) \sum_{j=1}^{N-2} (2D_j - 1) \cdot 2^{-j-1} + \frac{1}{2} \right] CV_{ref}^2. \quad (2)$$

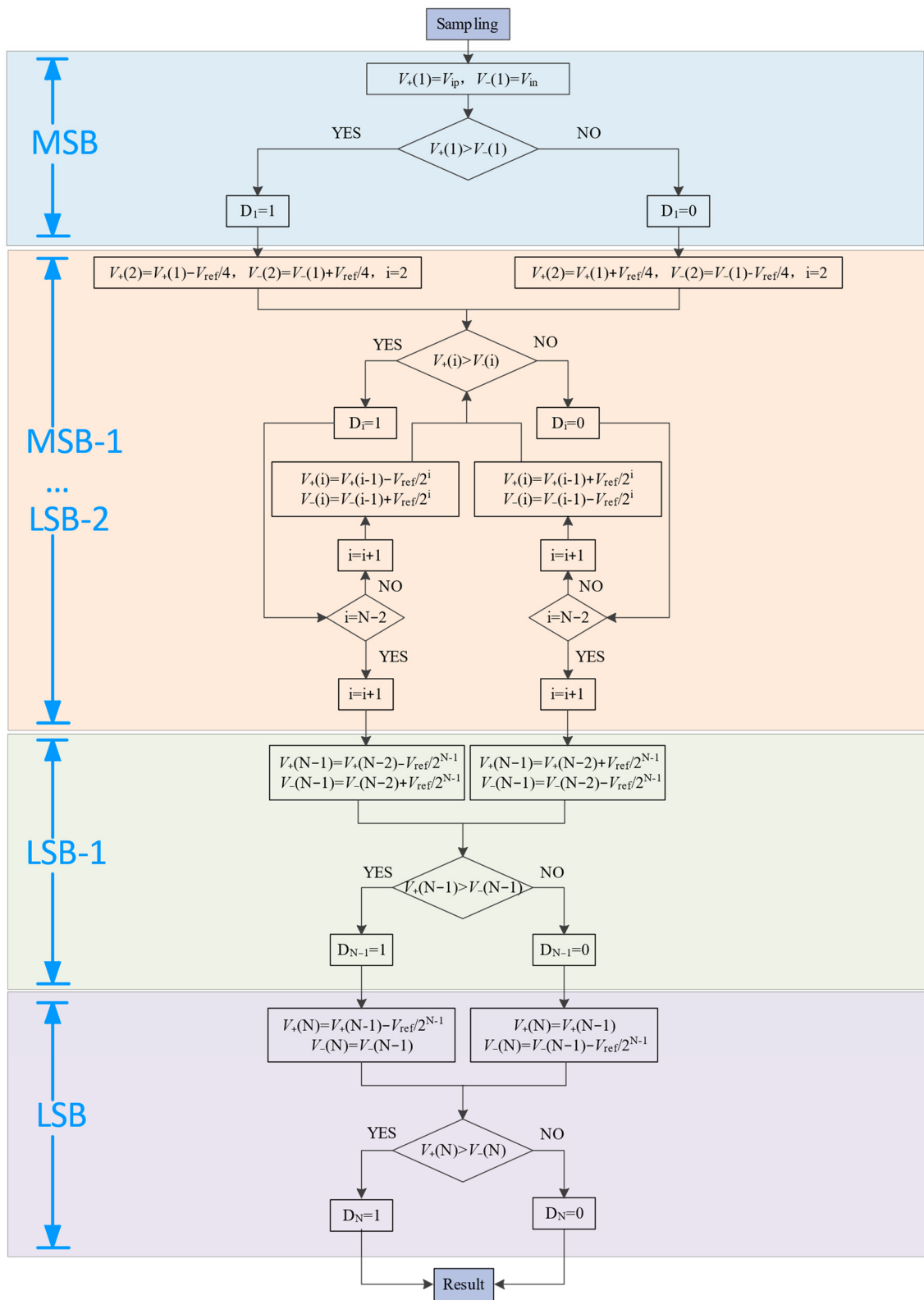
Nth Comparison: In this comparison, the last capacitor in the unit array connected to the higher voltage side is switched from  $V_{cm}$  to ground. Meanwhile, the capacitor on the lower voltage side remains unchanged, and the comparator outputs the result of the final comparison ( $D_N$ ). The switching energy of the capacitor array in this comparison is as follows:

$$E_N = \left[ D_{N-1} \cdot \sum_{j=1}^{N-2} (1 - D_j) \cdot 2^{-j-1} + (1 - D_{N-1}) \cdot \sum_{j=1}^{N-2} D_j \cdot 2^{-j-1} \right] CV_{ref}^2 \quad (3)$$

For N-bit resolution, assuming equal probability of each code appearance, the average switching energy of the capacitor array is as follows:

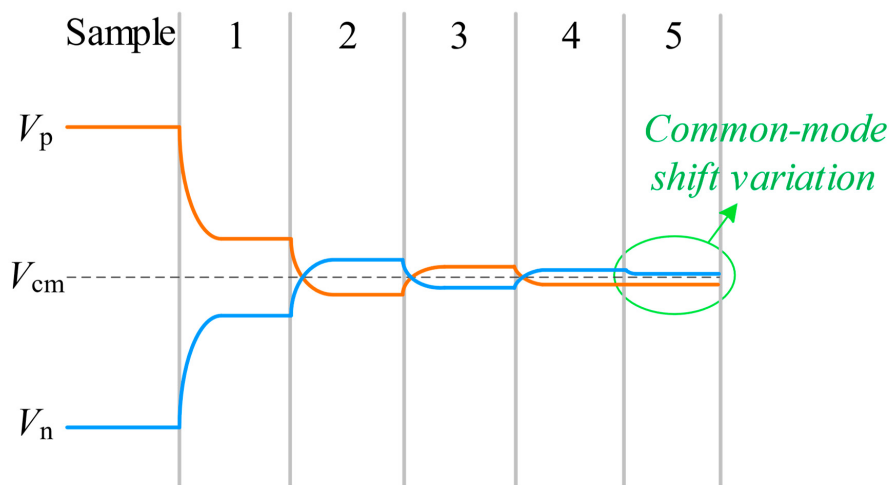
$$E_{\text{average}} = \left[ \sum_{i=2}^{N-1} (2^{N-i-2} - 2^{N-2i-1}) + 2^{-2} - 2^{-N} \right] CV_{ref}^2 \quad (4)$$

Figure 4's flowchart illustrates the proposed switching scheme. It depicts the comparator's role in determining the value of the  $i$ th bit by generating its corresponding reference voltage. The flowchart also details the DAC switching process, the comparison logic order, and the voltage offset of the capacitor array.



**Figure 4.** The flow chart of the proposed switching scheme.

Figure 5 displays the successive approximation waveforms of the suggested switching scheme. The common-mode voltage remains at  $V_{cm}$  from the initial comparison to the  $(N - 1)$ th comparison, with only the last comparison shifting the common-mode voltage by one LSB.



**Figure 5.** Waveform of the proposed switching scheme.

For a 10-bit case, the set and down based on capacitive top-plate sampling and the monotonic capacitor switching procedure reduces the average switching energy to  $255.5 CV_{ref}^2$ . The set and down [9] is more efficient than the conventional architecture, and the  $V_{cm}$ -based switching scheme [10] based on the common-mode charge recovery switching method and the use of a third reference voltage,  $V_{cm}$ , further reduce the switching energy. Wang et al. [11] applied a C-2C dummy capacitor based on the monotonic capacitor switching procedure. The HSRS switching scheme [12] in the first 2 MSBs, which account for a large proportion of energy consumption, achieves zero energy consumption without using any auxiliary circuit. Each of the above two switching schemes achieves 90.61% and 92.2% switching energy reduction compared with the conventional scheme. The shifted monotonic switching scheme (SMS) [13] achieves an average switching energy of  $63.75 CV_{ref}^2$  with a reduction of 75% compared to the set and down. Hu et al. [14] proposed a conversion scheme, reducing the switching energy consumption of all comparisons, except for the first 2 MSBs which do not consume switching energy. The average switching energy of the proposed capacitor-splitting low-complexity and energy-efficient switching scheme for a 10-bit SAR ADC is  $85.08 CV_{ref}^2$ . Compared to the conventional switching scheme [8], the average switching energy is reduced by 93.76%. Based on capacitor-splitting, additional reference voltage  $V_{cm}$ , and common-mode techniques, the proposed switching scheme does not achieve a lower switching energy than [13,14] but solves the problem of large common-mode voltage shift and high  $V_{cm}$  accuracy requirements, and achieves the trade-off between complexity and energy efficiency with low switching energy.

Various switching schemes for a 10-bit SAR ADC are simulated. The switching energy at each output code for different switching schemes is illustrated in Figure 6. The proposed scheme has more advantageous average switching energy.

Table 2 presents a comparison of various switching schemes for 10-bit SAR ADCs. These switching schemes [9,11–14] are highly energy-efficient but suffer from a significant common-mode shift or  $V_{cm}$  accuracy, which adversely affects DAC accuracy. In contrast, the proposed DAC switching scheme exhibits a common-mode shift of only one LSB, which is smaller than the common-mode shifts observed in switching schemes [11–14]. Moreover, the  $V_{cm}$  accuracy has a minimal impact on the DAC accuracy.

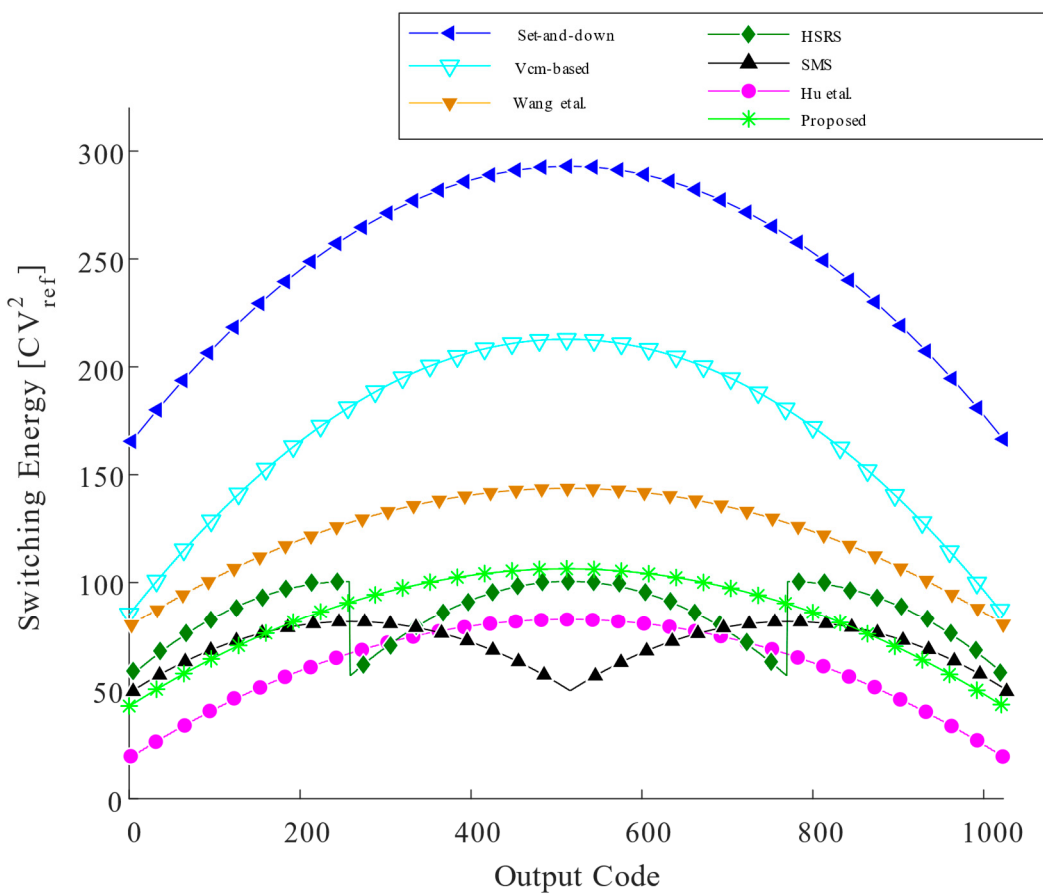


**Figure 6.** Switching energy against output codes [9–14].

**Table 2.** Comparison of different switching schemes of a 10-bit SAR ADC.

Switching Scheme	Average Energy ( $CV_{ref}^2$ )	Energy Saving (%)	Sensitivity to the Accuracy of $V_{cm}$	Number of References for Each Capacitor	Maximum Common-Mode Variation
Conventional [8]	1363.3	Reference	No	2	0 LSB
Monotonic [9]	255.5	81.26%	No	2	512 LSB
$V_{cm}$ -based [10]	170.2	87.52%	Very high	3	0 LSB
Wang et al. [11]	128	90.61%	No	2	512 LSB
HSRS [12]	106.2	92.20%	Very high	3	256 LSB
SMS [13]	63.75	95.32%	Very high	3	768 LSB
Hu et al. [14]	63.56	95.34%	Very low	2	256 LSB
Proposed	85.08	93.76%	Very low (only LSB and second LSB)	2 (all bits except second LSB)	1 LSB

## 2.2. Bootstrapped Sampling Switch

The proposed SAR ADC scheme is a differential structure; in order to improve the performance of the sampling switch and reduce the sampling error, the gate voltage bootstrap switch is used as the sampling switch. The differential sampling structure reduces the common-mode effect of the non-idealities of the bootstrap circuit [26], thereby increasing the accuracy of the sample-and-hold circuit. PMOS or NMOS switches have excessive on-resistance when the input signal is close to VDD or the ground and have poor linearity. In contrast, bootstrap switches possess on-resistance that remains constant regardless of the input signal amplitude, resulting in a higher degree of linearity [27] and a

higher spurious-free dynamic range (SFDR) value. The gate voltage bootstrap switch circuit structure is shown in Figure 7a.  $C_B$  represents the bootstrapped capacitor,  $C_H$  represents the sampling capacitor, and MS represents the sampling switch tube. The control logic of the sampling switch includes the reset switch, M4 control mechanism, and sampling control. The timing control logic details of the sampling switch are shown in Figure 7b, with the gate voltage bootstrapping process divided into two stages: sampling and holding.

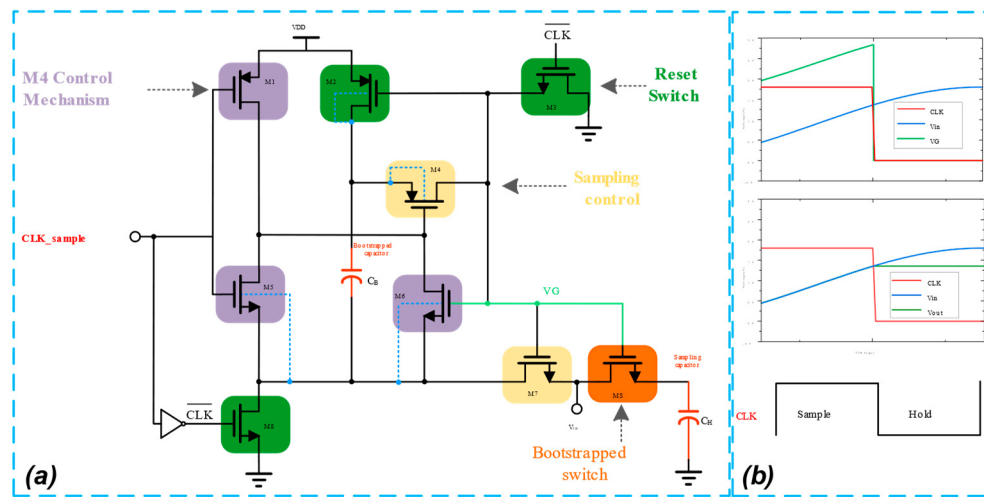


**Figure 7.** Bootstrapped sampling switch. (a) Bootstrapped sampling schematic. (b) Transient simulation.

**Sampling stage:** The sampling signal  $CLK\_sample$  is high, and the sampling switch is closed; M5 pulls down the gate potential of M4, and the voltage VDD on  $C_B$  is added to the gate of MS through the M4 tube so that the gate source voltage of MS maintains a constant voltage VDD independent of the input signal, and thus the on-resistance of the MS tubes maintains a constant value independent of  $V_{in}$ . Charge conservation is utilized for the gate capacitance of the MS, the  $C_B$ , and other parasitic capacitances, resulting in the voltage at the VG point being  $VDD + V_{in}$  and the output at the  $V_{OUT}$  side being  $V_{in}$ . It should be noted that the back gates of the M2 and M5 need to be connected to the upper board of the  $C_B$  in order to avoid the latch-up effect.

**Holding stage:** The sampling signal  $CLK\_sample$  is low, and the sampling switch is reset; M3 is turned on, and the gate potential of M2 is pulled down to zero scale, at which point the bootstrap switch MS is in the off state. At the same time, M2 and M8 are turned on and capacitor  $C_B$  is charged to VDD. During the charging of  $C_B$ , M4 and M7 isolate the capacitor from the switch MS, and the node VG is low.

The bootstrap switch is used to create a sample-and-hold circuit, and pre-simulation is performed. As depicted in Figure 8, the output waveform of sinusoidal time-domain transient simulation reveals that when the sampling signal  $CLK\_sample$  is high, the control signal VG of the sampling switch ascends in a bootstrap manner and fluctuates with the input signal  $V_{in}$ . The waveforms of VG and  $V_{in}$  essentially maintain a constant difference, i.e., the gate voltage of transistor MS remains unchanged with the input signal  $V_{in}$  during sampling. This reduces the sampling error and achieves the gate voltage bootstrap function required by the design.

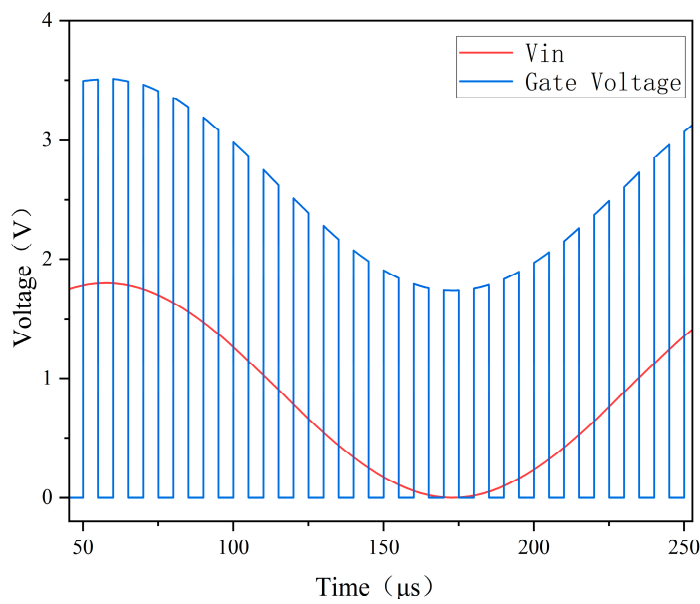


**Figure 8.** Simulation of bootstrapped sampling switch.

Figure 9 illustrates the spectral analysis results of the bootstrapped sampling switch. The FFT plot of the output waveform after the gate voltage bootstrap switch shows good noise suppression, with most of the bottom noise below  $-130$  dB. The signal-to-noise distortion ratio (SNDR) of the sampled output waveform is  $98.30$  dB, exhibiting good linearity and meeting the requirements of the designed 10-bit ADC. Additionally, the gate voltage bootstrap switch does not consume quiescent operating current, thereby having a small effect on the overall power consumption of the ADC. Consequently, the bootstrap switch design fulfills the necessary criteria.

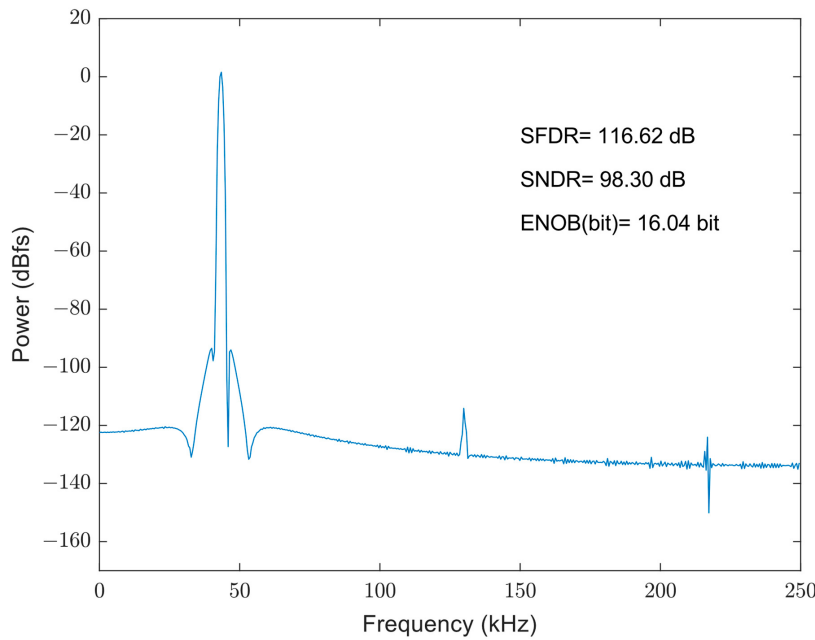


**Figure 9.** FFT of bootstrapped sampling switch.

### 2.3. Dynamic Comparator

As one of the key modules of the SAR ADC, the performance of the comparator, particularly its speed, power consumption, noise, and misalignment, significantly impacts the overall performance of the SAR ADC circuit and, consequently, the accuracy of the

SAR ADC's digital code output. Dynamic comparators are well suited for low-power, high-speed ADCs [28]. The proposed SAR ADC utilizes a dynamic comparator with self-shutdown control logic, employing a PMOS transistor input pair which offers improved noise immunity at higher operating frequencies [29], as shown in Figure 10a. In order to reduce the noise effect [30] and extend the signal amplification time, the comparator introduces three 50 ps delay buffers. During the comparison's initiation, only M1's switching action introduces minimal noise. Due to its lack of static current consumption, a dynamic comparator is suitable for an energy-efficient design. The comparator's operation is governed by various clock control signals: CLK\_comp manages the comparator's switching state, while CLK1 and CLK2 control the conduction state of the reset control tubes M7, M10, M6, and M11, and CLK3 governs the conduction state of the current source M1. The comparator's operation is divided into two stages: reset and comparison.

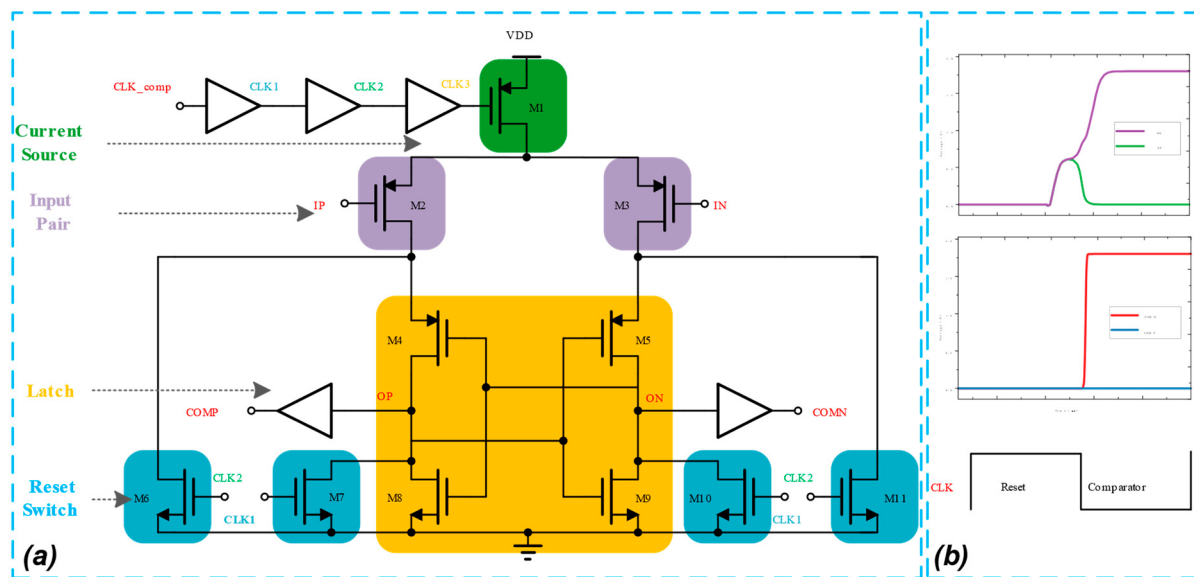


**Figure 10.** Simulation of dynamic comparator. (a) Comparator schematic. (b) Transient simulation.

Reset stage: The clock control signals are high, M1 is cut off, the path connecting ON and OP to VDD is disconnected, and the latch output is reset to a low state.

Comparison stage: The falling edge of CLK triggers the comparison process, with VDD charging the ON node through M1, M2, and M4, and the OP node through M1, M3, and M5. The speed of charging depends on the voltage of IP and IN. The input transistors compare input signals and collect charges on nodes OP and ON. If IP is greater than IN, varying currents flow into the cross-coupled inverters M4, M8 and M5, M9. Under the influence of positive feedback, the voltage in the final OP node will increase, while the ON node voltage will decrease, causing COMP to go high and COMN to go low. During comparator operation, if IP is less than IN, the output of the COMP will decrease, while the output of COMN will increase, resulting in a corresponding 0/1 output which completes the comparison process. Additionally, since there is no DC path from VDD to ground, only dynamic power is consumed.

The transient simulation of the comparator is depicted in Figure 10b. The differential input signals IP and IN are 925 mV and 875 mV, respectively. As CLK drops to a low level, the input transistors compare the input signals and accumulate charges on nodes OP and ON. Initially, OP and ON raise their voltages simultaneously. Subsequently, with positive feedback, eventually the OP node voltage increases and the ON node voltage decreases. Finally, the comparator generates the output of the comparison result, where one of COMP and COMN will be high and the other will be low.

## 2.4. Dynamic SAR Logic

The bit conversion of the SAR ADC is under the control of the SAR logic circuit. This circuit uses the comparator's output to determine the relevant digital bits and generates a control signal to switch the capacitor array to a new state. At the end of the bit-switching process, the logic block outputs all digital codes. Conventional SAR logic mainly consists of ring counters and shift registers, which require at least  $2N$  flip-flops with a large number of MOS tubes, resulting in high power consumption.

The proposed ADC employs dynamic SAR logic to reduce the overall power consumption. As shown in Figure 11c, the switching logic consists of a sequencer and a data register. The sequencer is a shift register that is signalized by a series of dynamic shift controllers (DSCs), as shown in Figure 11a. Once the shift operation is finished, the register's latch is activated using the set signal reset. The time sequences of the main clock, sampling clock, and digital output of the proposed SAR ADC are shown in Figure 11b. When the last dynamic shift controller in the sequencer turns on, it resets the sequencer and starts a new conversion cycle. The data register consists of dynamic latches that latch the comparator output from high to low. Dynamic latches can latch the differential output of the comparator and output the data differentially, simplifying the logic circuit. The latch schematic details are shown in Figure 11d.

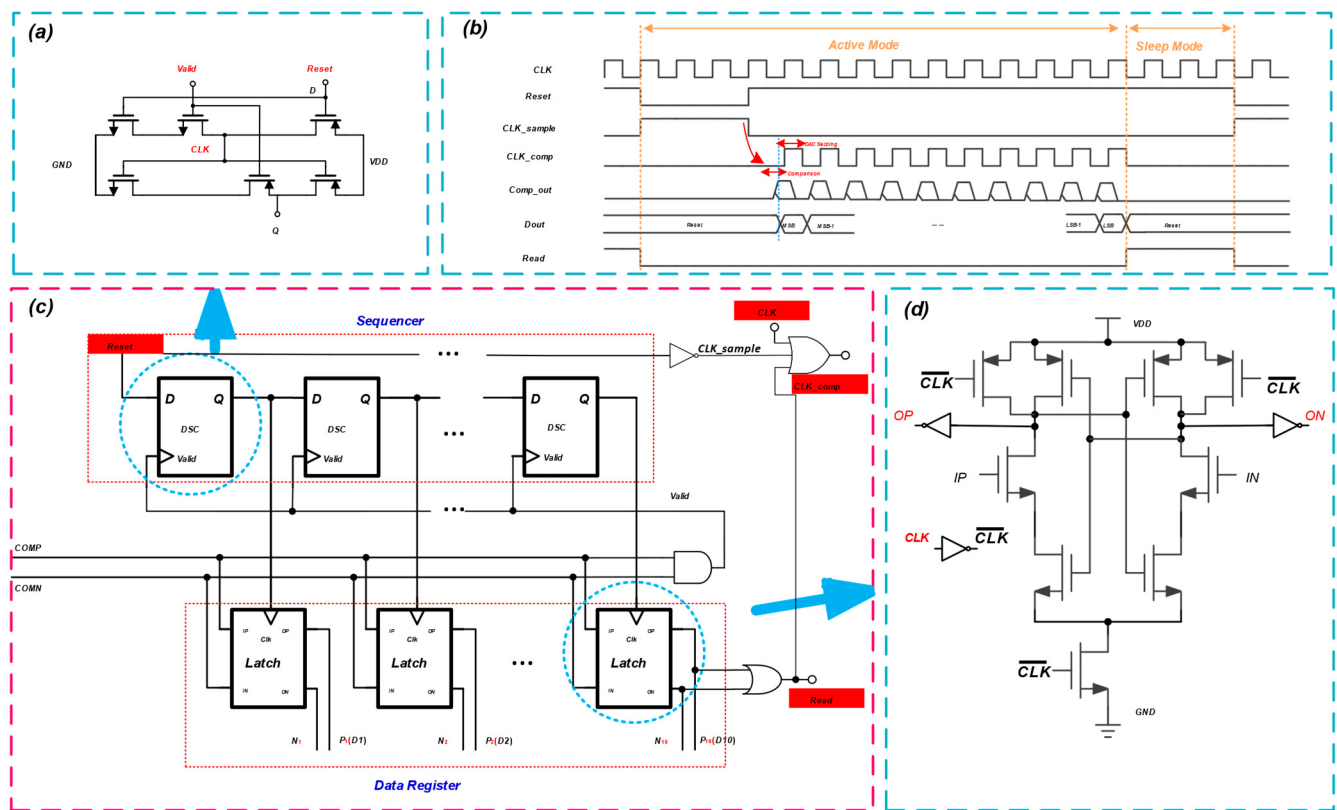


**Figure 11.** Dynamic SAR logic. (a) Dynamic shift controller schematic. (b) Timing diagram. (c) SAR logic schematic. (d) Latch schematic.

## 2.5. DAC Driver Circuit Design

The control logic circuit is implemented using logic gates and switches. Figure 12 depicts the control logic circuit of the DAC in a 10-bit SAR ADC with the proposed switching scheme. In order to reduce the complexity and power consumption of capacitive drive circuits, the CMOS inverters are mainly used for capacitive driving. Since the last two capacitors use  $V_{cm}$  as the reference voltage, the drive needs to add a transmission gate. Figure 12 outlines the drive circuitry and corresponding capacitance for every sub-array

in the DAC capacitor array.  $P_i$  and  $N_i$  refer to the comparison result of the  $i$ th ( $i = 1-10$ ) bit, where  $N_i$  is 0 when  $P_i$  is 1 and vice versa. The 1st bit represents the MSB in a 10-bit SAR ADC. The control logic is simple to implement thanks to the less complex switching scheme. Most of the capacitors are driven by a CMOS inverter structure, and the LSB-1 capacitor is driven by a hybrid structure combining a CMOS transmission gate and a CMOS inverter. Compared with the control logic in Refs. [10,12,13], the complexity of the control logic circuit for the proposed switching scheme is low. With the development of process technology, the power consumption and area of the control logic become small enough.

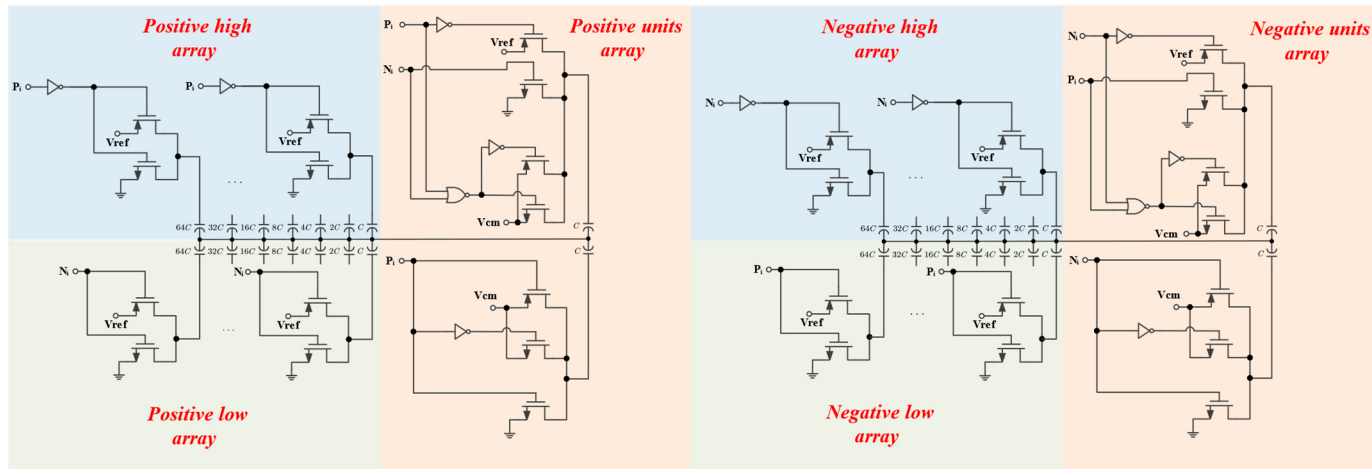


**Figure 12.** 10-bit SAR ADC control logic of the proposed switching scheme.

### 3. Analysis of Results

The SAR ADC was designed and simulated utilizing 180 nm CMOS technology. The size of the unit capacitance  $C$  in the capacitor array is set to  $4 \mu\text{m} \times 4 \mu\text{m}$ , and  $C = 17.2 \text{ fF}$ . According to the working principle of the logic analyzer, the logic analyzer function module is written in Verilog-A hardware description language for saving the simulation data and then processed.

The static parameters are tested using the Code Density Test (CDT) method [31]. The simulation parameters are as follows: the power supply is 1 V and the sampling rate is 200 kS/s. The simulated differential non-linearity (DNL) and integral non-linearity (INL) of the proposed SAR ADC are shown in Figure 13; the peak DNL and INL are  $-0.42 \text{ LSB} \sim +0.33 \text{ LSB}$  and  $-0.38 \text{ LSB} \sim +0.26 \text{ LSB}$ , respectively, which are less than 0.5 LSB, so the designed circuit satisfies the static characterization requirement. The static performance of the proposed SAR ADC is somewhat limited by capacitor mismatch resulting from process gradient errors.

Figure 14 shows the FFT spectrum of the proposed SAR ADC: the harmonic components are not significant. The ADC achieves a 78.06 dB spurious-free dynamic range (SFDR) and a 61.77 dB signal-to-noise and distortion ratio (SNDR), and the effective number of bits is 9.97 bits. The measured SFDRs demonstrate the good linearity of the proposed bootstrap S/H. The actual effective bits are affected by non-ideal factors, such as noise, misalignment, capacitance mismatch, etc., and the errors caused by these factors are within the acceptable range. Figure 15 shows the FFT of the SAR ADC for different process corners. The ADC achieves a 61.65 dB SNDR and a 77.10 dB SFDR at a process corner of FF, and a 61.69 dB SNDR and a 76.00 dB SFDR in the SS case, with the effective number of bits being 9.95 bits in both cases. Through the simulation and analysis of the process corners, it can be seen that the proposed scheme has a more stable performance under different process conditions, and the circuit has a certain degree of reliability.

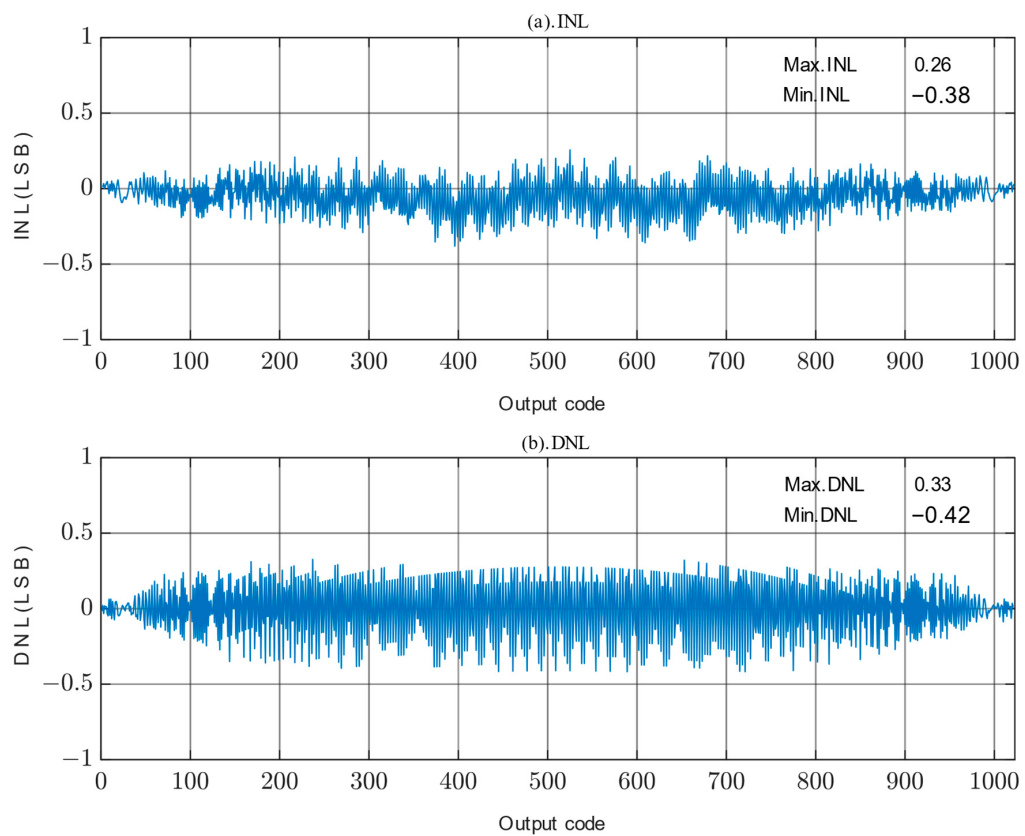


**Figure 13.** DNL and INL of proposed SAR ADC. (a) INL. (b) DNL.

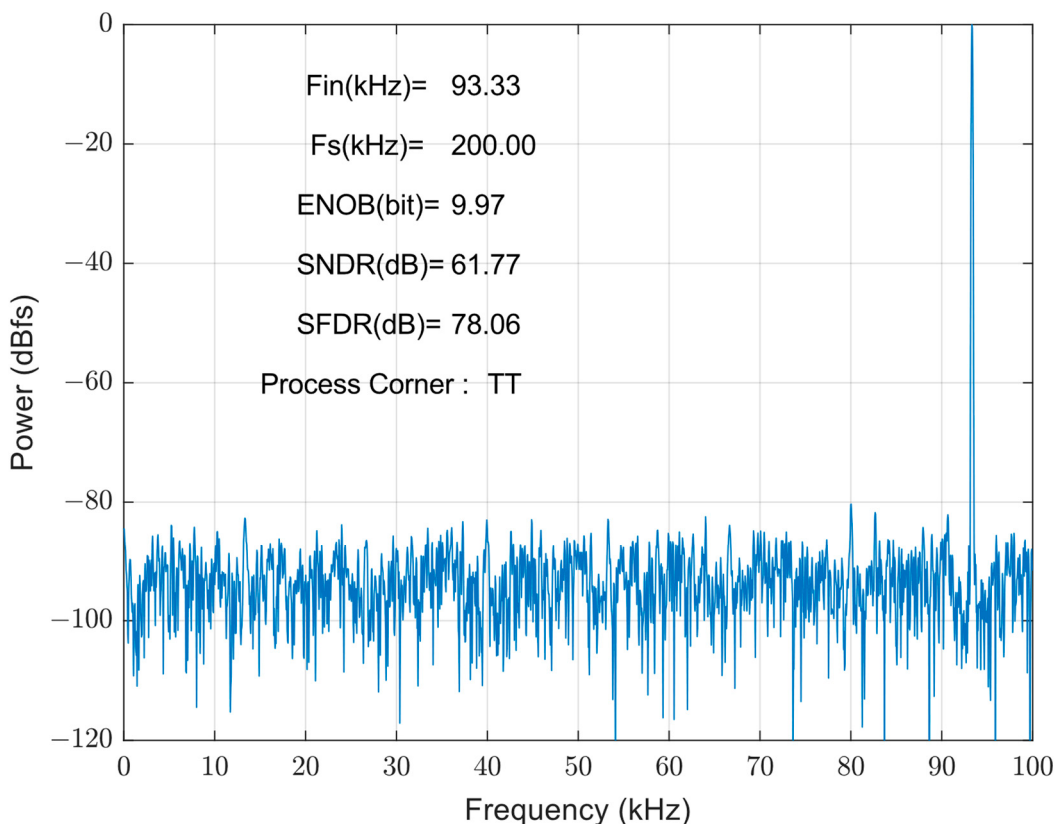


**Figure 14.** FFT of proposed SAR ADC at the TT process corner.

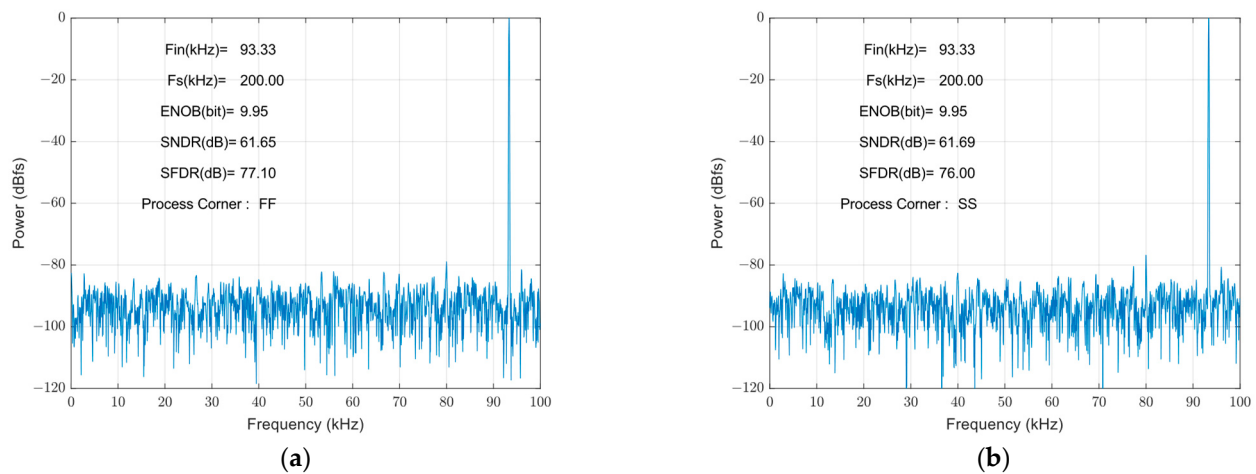


**Figure 15.** Process corner analysis: (a) FF process corner; (b) SS process corner.

The average total power consumption of the SAR ADC is approximately  $4.45 \mu\text{W}$ . Figure 16's pie chart displays the power consumption of each component, with the DAC and SAR dissipating the majority of the power. The comparison of the proposed ADC to other advanced SAR ADCs employs the figure of merit (FOM). According to [32], FOM is defined as follows:

$$\text{FOM} = \frac{\text{Power}}{2^{\text{ENOB}} \times F_s} \quad (5)$$

where  $F_s$  is the sampling frequency, and ENOB is the effective number of bits of the Nyquist input, while Power is the total power consumption of the SAR ADC. The proposed SAR ADC achieves an FOM of  $22.2 \text{ fJ/conv.-step}$ , which is competitive.

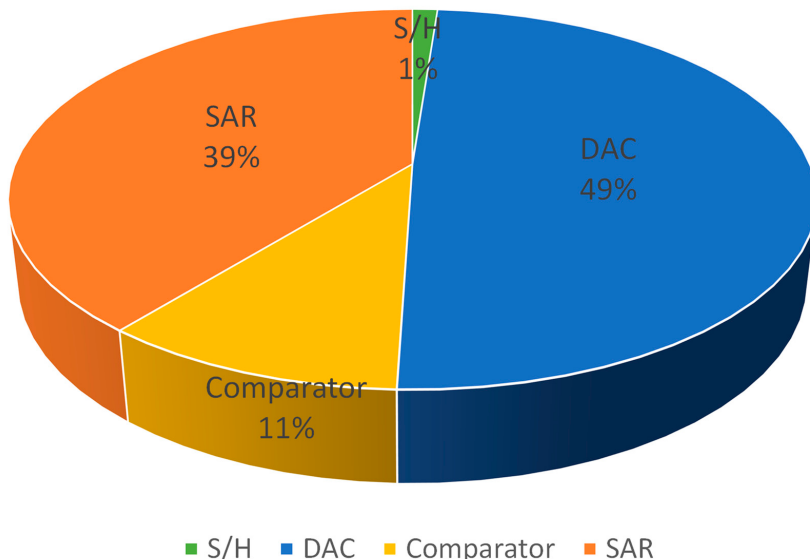


**Figure 16.** Power breakdown of proposed SAR ADC.

The performance summary of some SAR ADCs [21,22,33–36] along with the circuit-level simulation results of this work are summarized in Table 3. The suggested ADC is clearly more efficient in terms of power usage and other metrics. It is highly energy-efficient, low in complexity, and small in area. Therefore, this ADC is a more advantageous choice in power and area-constrained wearable biosensor systems. The proposed ADC has many application possibilities since many biosensor devices need to detect analog signals. Moreover, performance can be further improved by using more modern CMOS technology.

**Table 3.** Performance comparison of proposed SAR ADC.

Parameter	[21] *	[22] *	[33] *	[34]	[35]	[36] *	This Work *
Process (nm)	180	180	180	180	180	180	180
Resolution (bits)	14	10	10	12	10	10	10
Sampling Rate (MS/s)	0.01	1	1	0.1	0.5	2	0.2
Supply Voltage (V)	1.8	0.5	1.8	1	1	1.8	1
SNDR (dB)	84.50	61.96	58.9	65.3	57.38	59.59	61.77
ENOB (bits)	13.80	7.69	9.5	10.55	9.24	9.65	9.97
DNL (LSB)	0.5	−0.82/0.9	−0.40/0.36	−0.19/0.19	−0.72/0.50	−0.23/0.23	−0.42/0.33
INL (LSB)	0.42	−1.31/1.06	−0.46/0.36	−0.16/0.16	−0.88/0.85	−0.23/0.23	−0.38/0.26
Power Consumption ( $\mu$ W)	19.5	13.99	131	25	14.2	41.92	4.45
FOM (fJ/conv. Step)	140	67.7	181	165	47	26.9	22.2

\* Simulated results.

#### 4. Conclusions

This paper presents a low-power SAR ADC designed for high-efficiency wearable biosensor applications. The utilization of a capacitor-splitting energy-efficient switching scheme effectively reduces energy consumption. Based on capacitor-splitting, additional reference voltage  $V_{cm}$ , and common-mode techniques, the proposed switching scheme achieves 93.76% less switching energy compared to the conventional scheme. Furthermore, most of the capacitors have only two reference voltages, accomplishing low complexity, and the accuracy of  $V_{cm}$  has a very low impact on the accuracy of the DAC. The proposed DAC switching scheme has a common-mode shift of one LSB, reducing the design complexity of the comparator. In addition, the simulation results demonstrate that the ADC achieves a 61.77 dB SNDR and a 78.06 dB SFDR and consumes 4.45  $\mu$ W of power in a 180 nm process with a 1 V power supply, a full-swing input signal frequency of 93.33 kHz, and a sampling rate of 200 kS/s.

**Author Contributions:** Conceptualization, Y.H.; methodology, Y.H.; software, Y.H. and Q.H.; validation, Y.H., Q.H., and C.C.; formal analysis, Y.H. and Q.H.; investigation, L.H. and E.Y.; resources, Y.H., B.L., and Z.W.; data curation, Q.H. and B.T.; writing—original draft preparation, Y.H. and Q.H.; writing—review and editing, B.T., C.C., and L.H.; visualization, Q.H., B.T., and E.Y.; supervision, Y.H.; project administration, Y.H., Q.H., and Z.W.; funding acquisition, B.L. and Y.H. All authors have read and agreed to the published version of the manuscript.

**Funding:** This work is funded by the National Natural Science Foundation of China (No. 60976026), the Key Field Project of Colleges and Universities in Guangdong Province (No. 2021ZDZX1081), the Key Project of Social Welfare and Basic Research Project in Zhongshan City (2021B2020), the Construction Project of Professional Quality Engineering in 2020 (No. YLZY202001), and the Construction Project of Professional Quality Engineering in 2021 (No. JD202101).

**Data Availability Statement:** Data are contained within the article.

**Conflicts of Interest:** The authors declare no conflict of interest.

#### References

- Tai, H.-Y.; Hu, Y.-S.; Chen, H.-W.; Chen, H.-S. 11.2 A 0.85fJ/Conversion-Step 10b 200kS/s Subranging SAR ADC in 40nm CMOS. In Proceedings of the 2014 IEEE International Solid-State Circuits Conference Digest of Technical Papers (ISSCC), San Francisco, CA, USA, 9–13 February 2014; pp. 196–197.
- Kim, H.; Kim, S.; Van Helleputte, N.; Artes, A.; Konijnenburg, M.; Huisken, J.; Van Hoof, C.; Yazicioglu, R.F. A Configurable and Low-Power Mixed Signal SoC for Portable ECG Monitoring Applications. *IEEE Trans. Biomed. Circuits Syst.* **2014**, *8*, 257–267. [[CrossRef](#)]
- Zhao, X.; Li, D.; Zhang, X.; Liu, S.; Zhu, Z. A 0.6-V 94-nW 10-Bit 200-kS/s Single-Ended SAR ADC for Implantable Biosensor Applications. *IEEE Sens. J.* **2022**, *22*, 17904–17913. [[CrossRef](#)]
- Yuan, C.; Ng, K.A.; Xu, Y.P.; Yen, S.-C.; Thakor, N.V. A 1-V 9.8-ENOB 100-kS/s Single-Ended SAR ADC with Symmetrical DAC Switching Technique for Neural Signal Acquisition. In Proceedings of the 2015 IEEE Asian Solid-State Circuits Conference (A-SSCC), Xia'men, China, 9–11 November 2015; pp. 1–4.
- Aneesh, K.; Manoj, G.; Shyli Sam, S. Design Approaches of Ultra-Low Power SAR ADC for Biomedical Systems—A Review. *J. Circuit Syst. Comput.* **2022**, *31*, 2230009. [[CrossRef](#)]

6. Tyagi, M.; Mittal, P.; Kumar, P. Design of 8 -Bit Low Power SAR ADC in 45 Nm for Biomedical Implants. *Phys. Scr.* **2023**, *98*, 116101. [[CrossRef](#)]
7. Tong, X.; Ghovanloo, M. Energy-efficient Switching Scheme in SAR ADC for Biomedical Electronics. *Electron. Lett.* **2015**, *51*, 676–678. [[CrossRef](#)]
8. McCreary, J.L.; Gray, P.R. All-MOS Charge Redistribution Analog-to-Digital Conversion Techniques. I. *IEEE J. Solid-State Circuits* **1975**, *10*, 371–379. [[CrossRef](#)]
9. Liu, C.-C.; Chang, S.-J.; Huang, G.-Y.; Lin, Y.-Z. A 10-Bit 50-MS/s SAR ADC With a Monotonic Capacitor Switching Procedure. *IEEE J. Solid-State Circuits* **2010**, *45*, 731–740. [[CrossRef](#)]
10. Zhu, Y.; Chan, C.-H.; Chio, U.-F.; Sin, S.-W.; Seng-Pan, U.; Martins, R.P.; Maloberti, F. A 10-Bit 100-MS/s Reference-Free SAR ADC in 90 Nm CMOS. *IEEE J. Solid-State Circuits* **2010**, *45*, 1111–1121. [[CrossRef](#)]
11. Wang, H.; Zhu, Z. Energy-Efficient and Reference-Free Monotonic Capacitor Switching Scheme with Fewest Switches for SAR ADC. *IEICE Electron. Express* **2015**, *12*, 20141202. [[CrossRef](#)]
12. Zhang, H.; Zhang, H.; Zhang, R. Energy-efficient Higher-side-reset-and-set Switching Scheme for SAR ADC. *Electron. Lett.* **2017**, *53*, 1238–1240. [[CrossRef](#)]
13. Hsieh, S.-E.; Hsieh, C.-C. A 0.3-V 0.705-fJ/Conversion-Step 10-Bit SAR ADC with a Shifted Monotonic Switching Procedure in 90-Nm CMOS. *IEEE Trans. Circuits Syst. II* **2016**, *63*, 1171–1175. [[CrossRef](#)]
14. Hu, Y.; Yi, Z.; He, Z.; Li, B. Energy-Efficient, Area-Efficient, High-Accuracy and Low-Complexity Switching Scheme for SAR ADC. *IEICE Electron. Express* **2017**, *14*, 20170428. [[CrossRef](#)]
15. Yang, C.; Olieman, E.; Litjes, A.; Qiu, L.; Tang, K.; Zheng, Y.; Van Veldhoven, R. An Area-Efficient SAR ADC With Mismatch Error Shaping Technique Achieving 102-dB SFDR 90.2-dB SNDR Over 20-kHz Bandwidth. *IEEE Trans. VLSI Syst.* **2021**, *29*, 1575–1585. [[CrossRef](#)]
16. Zhang, H.; Zhang, H.; Sun, Q.; Li, J.; Liu, X.; Zhang, R. A 0.6-V 10-Bit 200-kS/s SAR ADC With Higher Side-Reset-and-Set Switching Scheme and Hybrid CAP-MOS DAC. *IEEE Trans. Circuits Syst. I* **2018**, *65*, 3639–3650. [[CrossRef](#)]
17. Jian, M.; Zheng, J.; Kong, X.; Yuan, M.; Zhang, C.; Guo, C.; Sun, B. A 12-Bit SAR ADC with a Reversible VCM-Based Capacitor Switching Scheme. *Microelectron. J.* **2022**, *129*, 105588. [[CrossRef](#)]
18. Tong, X.; Zhao, S.; Xin, X. High Energy Efficiency and Linearity Switching Scheme Without Reset Energy for SAR ADC. *Circuits Syst. Signal Process.* **2022**, *41*, 5872–5894. [[CrossRef](#)]
19. Huang, L.; Li, J.; Jiang, X.; Wu, J. A 2.1-fJ/Conversion-Step 10-Bit 125-KS/s SAR ADC with Vcm-Based Bidirectional Single-Side Switching Scheme. In Proceedings of the 2023 12th International Conference on Modern Circuits and Systems Technologies (MOCAST), Athens, Greece, 28–30 June 2023; pp. 1–4.
20. Wu, Y.; Cheng, X.; Zeng, X. A 960  $\mu$ W 10-Bit 70-MS/s SAR ADC with an Energy-Efficient Capacitor-Switching Scheme. *Microelectron. J.* **2013**, *44*, 1260–1267. [[CrossRef](#)]
21. Mekkattillam, Y.; Mohapatra, S.; Mohapatra, N.R. Design and Calibration of 14-Bit 10 KS/s Low Power SAR ADC for Bio-Medical Applications. In *VLSI Design and Test*; Sengupta, A., Dasgupta, S., Singh, V., Sharma, R., Kumar Vishvakarma, S., Eds.; Communications in Computer and Information Science; Springer Singapore: Singapore, 2019; Volume 1066, pp. 590–604. ISBN 978-981-329-766-1.
22. Mandrumaka, K.K.; Noorbasha, F. A Low Power 10 Bit SAR ADC with Variable Threshold Technique for Biomedical Applications. *SN Appl. Sci.* **2019**, *1*, 918. [[CrossRef](#)]
23. Lin, J.-Y.; Hsieh, C.-C. A 0.3 V 10-Bit 1.17 f SAR ADC With Merge and Split Switching in 90 Nm CMOS. *IEEE Trans. Circuits Syst. I* **2015**, *62*, 70–79. [[CrossRef](#)]
24. Huang, G.-Y.; Chang, S.-J.; Liu, C.-C.; Lin, Y.-Z. 10-Bit 30-MS/s SAR ADC Using a Switchback Switching Method. In *IEEE Transactions on Very Large Scale Integration (VLSI) Systems*; IEEE: Piscataway, NJ, USA, 2013; Volume 21, pp. 584–588. [[CrossRef](#)]
25. Promitzer, G. 12 Bit Low Power Fully Differential Switched Capacitor Non-Calibrating Successive Approximation ADC with 1MS/s. In Proceedings of the 26th European Solid-State Circuits Conference, Stockholm, Sweden, 19–21 September 2000; pp. 176–179.
26. Sengupta, S. Analytical Expression of HD3 Due to Non-Linear MOS Switch in MOSFET-C Sample and Hold Circuits. In Proceedings of the 2005 IEEE International Symposium on Circuits and Systems, Kobe, Japan, 23–26 May 2005; Volume 3, pp. 2251–2254.
27. Lin, K.-T.; Cheng, Y.-W.; Tang, K.-T. A 0.5 V 1.28-MS/s 4.68-fJ/Conversion-Step SAR ADC With Energy-Efficient DAC and Trilevel Switching Scheme. *IEEE Trans. VLSI Syst.* **2016**, *24*, 1441–1449. [[CrossRef](#)]
28. Rezapour, A.; Shamsi, H.; Abbasizadeh, H.; Lee, K.-Y. Low Power High Speed Dynamic Comparator. In Proceedings of the 2018 IEEE International Symposium on Circuits and Systems (ISCAS), Florence, Italy, 27–30 May 2018; pp. 1–5.
29. Khorami, A.; Sharifkhani, M. A Low-Power High-Speed Comparator for Precise Applications. In *IEEE Transactions on Very Large Scale Integration (VLSI) Systems*; IEEE: Piscataway, NJ, USA, 2018; Volume 26, pp. 2038–2049. [[CrossRef](#)]
30. Hussain, S.; Kumar, R.; Trivedi, G. Comparison of NMOS and PMOS Input Driving Dynamic Comparator in 45nm Technology. *IOP Conf. Ser. Mater. Sci. Eng.* **2021**, *1020*, 012022. [[CrossRef](#)]
31. Doernberg, J.; Lee, H.-S.; Hodges, D.A. Full-Speed Testing of A/D Converters. *IEEE J. Solid-State Circuits* **1984**, *19*, 820–827. [[CrossRef](#)]

32. Tong, X.; Song, M.; Chen, Y.; Dong, S. A 10-Bit 120 kS/s SAR ADC without Reset Energy for Biomedical Electronics. *Circuits Syst. Signal Process.* **2019**, *38*, 5411–5425. [[CrossRef](#)]
33. Saisundar, S.; Cheong, J.H.; Je, M. A 1.8V 1MS/s Rail-to-Rail 10-Bit SAR ADC in 0.18  $\mu\text{m}$  CMOS. In Proceedings of the 2012 IEEE International Symposium on Radio-Frequency Integration Technology (RFIT), Singapore, 21–23 November 2012; pp. 83–85.
34. Verma, N.; Chandrakasan, A.P. An Ultra Low Energy 12-Bit Rate-Resolution Scalable SAR ADC for Wireless Sensor Nodes. *IEEE J. Solid-State Circuits* **2007**, *42*, 1196–1205. [[CrossRef](#)]
35. Huang, H.-Y.; Lin, J.-Y.; Hsieh, C.-C.; Chang, W.-H.; Tsai, H.-H.; Chiu, C.-F. A 9.2b 47fJ/Conversion-Step Asynchronous SAR ADC with Input Range Prediction DAC Switching. In Proceedings of the 2012 IEEE International Symposium on Circuits and Systems, Seoul, Republic of Korea, 20–23 May 2012; pp. 2353–2356.
36. Fu, Z.; Tang, X.; Li, D.; Wang, J.; Basak, D.; Pun, K.-P. A 10-Bit 2 MS/s SAR ADC Using Reverse VCM-Based Switching Scheme. In Proceedings of the 2016 IEEE International Symposium on Circuits and Systems (ISCAS), Montréal, QC, Canada, 22–25 May 2016; pp. 1030–1033.

**Disclaimer/Publisher’s Note:** The statements, opinions and data contained in all publications are solely those of the individual author(s) and contributor(s) and not of MDPI and/or the editor(s). MDPI and/or the editor(s) disclaim responsibility for any injury to people or property resulting from any ideas, methods, instructions or products referred to in the content.